Wolf, Claus Christian ; Mertens, Christoph ; Gardner, Anthony D. ; Dollinger, Christoph ; Fischer, Andreas

# Optimization of differential infrared thermography for unsteady boundary layer transition measurement

# Optimization of differential infrared thermography for unsteady boundary layer transition measurement

C. Christian Wolf[1] · Christoph Mertens[1] · Anthony D. Gardner[1] · Christoph Dollinger[2] · Andreas Fischer[2]

## Abstract

Differential infrared thermography (DIT) is a method of analyzing infrared images to measure the unsteady motion of the laminar–turbulent transition of a boundary layer. It uses the subtraction of two infrared images taken with a short-time delay. DIT is a new technique which already demonstrated its validity in applications related to the unsteady aerodynamics of helicopter rotors in forward flight. The current study investigates a pitch-oscillating airfoil and proposes several optimizations of the original concept. These include the extension of DIT to steady test cases, a temperature compensation for long-term measurements, and a discussion of the proper infrared image separation distance. The current results also provide a deeper insight into the working principles of the technique. The results compare well to reference data acquired by unsteady pressure transducers, but at least for the current setup DIT results in an additional measurement-related lag for relevant pitching frequencies.

### Graphical abstract

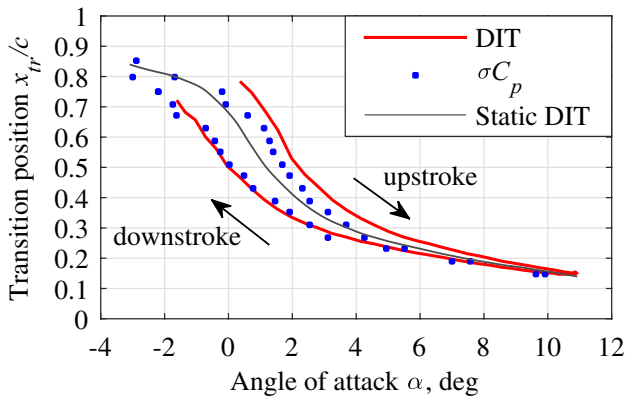


### Abbreviations

| | |
|---|---|
| 1MG | One-meter wind-tunnel Göttingen |
| DIT | Differential infrared thermography |
| DLR | German Aerospace Center |
| IT | Infrared thermography |

### List of symbols

| | |
|---|---|
| $c$ | Chord length, $c = 0.3$ m |
| $c_f$ | Skin-friction coefficient |
| $c_l$ | Lift coefficient |
| $c_p$ | Pressure coefficient |
| $C$ | Fluid specific heat capacity, J/m$^3$/K |
| $f$ | Pitching frequency, Hz |
| $k$ | Reduced frequency, $k = \pi fc/V_\infty$ |
| $M_\infty$ | Freestream Mach number |
| $\dot{q}_c$ | Convective heat flux, W/m$^3$ |

✉ C. Christian Wolf
christian.wolf@dlr.de

[1] German Aerospace Center (DLR), Institute of Aerodynamics and Flow Technology, Bunsenstr. 10, 37073 Göttingen, Germany

[2] Bremen Institute for Metrology, Automation and Quality Science (BIMAQ), University of Bremen, Linzer Strasse 13, 28359 Bremen, Germany

| | |
|---|---|
| Re | Reynolds number |
| $t$ | Time, s |
| $T$ | Airfoil surface temperature, K or counts |
| $T_\infty$ | Freestream temperature, K |
| $V_\infty$ | Freestream velocity, m/s |
| $x$ | Coordinate along the airfoil's chord line, m |
| $x_{tr}$ | Transition position, m |

**Greek symbols**

| | |
|---|---|
| $\alpha$ | Geometric angle of attack, deg |
| $\overline{\alpha}$ | Mean value of the angle of attack, deg |
| $\hat{\alpha}$ | Amplitude of the angle of attack, deg |
| $\Delta$ | Difference between two values |
| $\Delta T_p$ | DIT peak height, counts |
| $\rho$ | Density, kg/m$^3$ |
| $\sigma C_p$ | Standard deviation of the pressure coefficient |

## 1 Introduction

Boundary layer transition affects the aerodynamic performance of aircraft due to the different levels of skin friction in the laminar and turbulent regimes. Aircraft design, therefore, strives to control the amount of laminar flow over a wetted surface. This also holds true for the design of helicopter rotors (Coder 2017; Overmeyer and Martin 2017a; Vieira et al. 2017), but the flow structure is very complex when considering the periodically changing conditions on the advancing and retreating sides of a rotor in forward flight. An experimental study of this phenomenon must, therefore, be capable of measuring the unsteady motion of the transition region.

In contrast to this, the prediction and experimental determination of the static transition location under steady flow conditions have reached a high level of maturity, which also cover rotors in hover. Available experimental methods include infrared thermography as applied on model rotors (Overmeyer and Martin 2017b) or full-scale helicopter rotors (Richter and Schülein 2014; Richter et al. 2016a), chemical sublimation techniques (Tanner and Yaggy 1966), skin-friction oil interferometry (Schülein 2014; Wadcock et al. 1999), or temperature-sensitive paint (Weiss et al. 2017).

Unsteady transition, as encountered by a rotor in forward flight, requires experimental techniques with small response times, for example, hot-film setups. This method was applied both on pitching airfoils, see Goerttler et al. (2017), Lorber and Carta (1992), Richter et al. (2016b), and Schreck et al. (1998), and model rotors in simulated forward flight, see Raffel et al. (2011). A rather new approach is the analysis of the cycle-to-cycle variation of dynamic pressure transducer signals, which is termed "$\sigma C_p$" (Gardner and Richter 2015, 2016) and used as a reference in the current measurements. The response frequency of hot-film sensors and dynamic pressure transducers is in the high-kHz range and much larger than the application frequency, which for full-scale helicopters is typically in the range of 5–8Hz. They measure the transition position and its aerodynamic hysteresis without the introduction of additional measurement-related time delays. On the downside, all methods based on individual sensors have a limited spatial resolution, and the sensor integration into rotor blades is very complicated. These shortcomings motivated the development of the differential infrared thermography (DIT).

The DIT technique was proposed by Raffel and Merz (2014) and Raffel et al. (2015), who demonstrated the concept for both pitching airfoils and rotor blades. The surfaces were radiation-heated using spotlights to study the different convective heat transfer in the laminar and turbulent boundary layer regimes. The fundamental idea of DIT is to subtract two infrared images taken with a small time separation to visualize short-time events such as transition motion and to cancel out the time-averaged temperature distribution. Richter et al. (2016b) later compared DIT to hot-film sensors and pressure transducers on a pitching airfoil. The study underlined the validity of DIT, but also revealed some problems. These include the introduction of an additional time/phase lag in comparison with the well-established fast-response methods, and an erroneous behavior at the reversal points of the transition motion. Gardner et al. (2017) used a numerical simulation of the airfoil's thermal response to understand the measurement-related lag, showing that the separation of the subtracted infrared images is crucial for the accuracy of the method. The first application to a large-scale rotor in simulated forward flight was presented by Overmeyer et al. (2018). In this study, DIT showed that the boundary layer on the blade's lower surface switches between laminar and turbulent states and that the turbulent wake of trip dots follows the flow incidence angle at different azimuth positions. The authors also stress that a comparison to reference transition data from well-established techniques is desirable to support the understanding of the complex flow patterns. Gardner et al. (2016) and Raffel et al. (2017) extended the DIT measurement principle to detect unsteady flow separation in addition to the transition motion.

The current study aims to improve the fundamental understanding of DIT and to optimize the experimental procedure and the data processing algorithms. Therefore, a pitching airfoil is investigated rather than a rotor blade, since this simplifies the experimental setup and promotes the acquisition of a large data set with a variation of multiple parameters. The basic DIT principle is revisited for constant-pitch test cases with an angle-of-attack variation, underlining that the method is also a useful tool for steady or quasi-steady boundary layer transition detection. The static results are then compared to unsteady test cases, and the

influence of the data evaluation on the quality of the results is discussed in detail.

## 2 Experimental setup

The current study investigates the boundary layer transition on the suction side of a quasi-two-dimensional airfoil with a similar experimental setup to that chosen by Gardner et al. (2016), who focused on dynamic stall detection using differential infrared thermography. An instrumented wind-tunnel model (Richter et al. 2016b) with the DSA-9A helicopter airfoil, see Fig. 1, was installed into the open test section of the "one-meter wind tunnel" (1MG) at the German Aerospace Center (DLR) in Göttingen, see Fig. 2.

The airfoil has a chord length of $c = 0.3$ m and a span of 0.997 m, it was equipped with end plates to improve the two-dimensionality of the flow. The freestream velocity was set to $V_\infty = 50$ m/s ($M_\infty = 0.14$, $Re = 1.0 \cdot 10^6$). The freestream turbulence level at this $V_\infty$ is in the range between 0.15 and 0.20%. An electric actuation mechanism developed by Merz et al. (2017) was used to rotate the airfoil around its quarter chord for both constant-pitch test cases and pitching test cases with sinusoidal-motion parameters:

$$\alpha(t) = \overline{\alpha} - \widehat{\alpha} \cdot \cos(2\pi\, tf). \tag{1}$$

In this definition, the minimum angle of attack $\alpha$ is at phases of $tf = 0$ and 1, whereas the maximum angle of attack $\alpha$ is at $tf = 0.5$. The notation will be abbreviated in the following sections. For example, "$\alpha = 4° \pm 7°$" refers to a pitch motion with a mean of $\overline{\alpha} = 4°$ and an amplitude of $\widehat{\alpha} = 7°$. A summary of the parameter range considered in this study is given in Table 1. The geometric blockage of the open test section is between 4 and 9% depending on the airfoil's pitch angle.

The airfoil was equipped with 50 Kulite® pressure transducers, whose positions were optimized with a view to the lift coefficient discretization error (Richter et al. 2016b), see the red marks in Fig. 1. The signals of the pressure transducers were acquired through a data recorder at a sample rate of 200 kHz. For each test condition, the pressure data were recorded for 10 s (static cases) or 50 s (dynamic cases). The airfoil's geometric angle of attack $\alpha$ as measured by laser triangulators and the status signals of the infrared system were

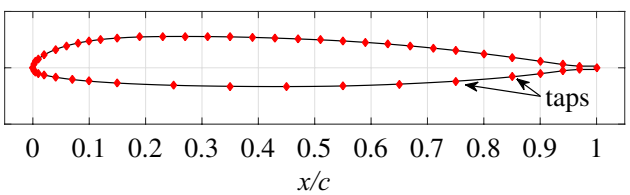


**Fig. 1** DSA-9A airfoil geometry and pressure tap distribution, reproduced from Richter et al. (2016b)

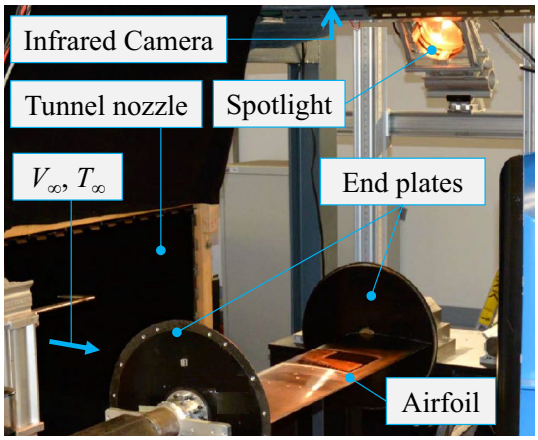


**Fig. 2** Picture of the setup in the wind-tunnel's open test section

stored simultaneously to synchronize the different measurement systems.

The high-speed infrared camera "FLIR SC7750-L" features a cadmium–mercury–telluride sensor with a spectral range of $8.0 - 9.4$ µm and a size of $640 \times 512$ px. The camera was mounted 2 m above the airfoil, see Fig. 3, and equipped with a 50 mm focal length lens. The image integration time was set to 190 µs, which is small enough to freeze the airfoil's motion for the studied pitch parameters. The image acquisition frequency of the infrared camera, 99.98 Hz, is slightly de-tuned to integral multiples of the airfoil's pitching frequencies. The infrared images are, therefore, not phase-locked, but slowly sweep through the airfoil's pitch cycle. Assuring that a sufficient number of pitch cycles per test point are recorded and that cycle-to-cycle differences are negligible, this results in a high resolution of the pitch phase with $\Delta tf = 2 \times 10^{-4}$ and allows for a systematic study of the influence of the DIT image separation distance.

A spotlight with a power output of up to 1500 W was mounted next to the infrared camera. The radiative heat

**Table 1** Variation of experimental parameters, default values are printed in bold letters

| Parameter | Value or range |
|---|---|
| Mean pitch $\overline{\alpha}$, deg | **4** (static: $-4 \ldots 12.5$) |
| Pitch amplitude $\widehat{\alpha}$, deg | 1, 2, 3, 4, 5, 6, **7**, 8 |
| Freestream vel. $V_\infty$, m/s | **50** |
| Pitch freq. $f$, Hz | 0.25, 0.5, 1, 2, **4**, 8 |
| Red. freq. $k = \pi fc/V_\infty$ | 0.005, 0.009, 0.019, 0.038, **0.075**, 0.151 |
| No. of infrared images | Static: 1000<br>Dynamic: **5000** |
| Heating $T - T_\infty$, K | Static: ca. 5–6<br>Dynamic: ca. **10–12** |

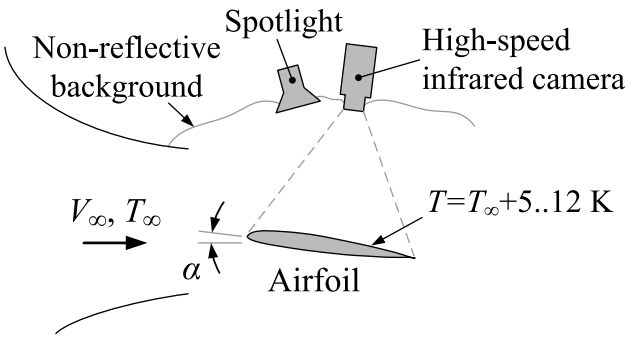


**Fig. 3** Sketch of the wind-tunnel setup, not to scale, reproduced from Gardner and Richter (2016)

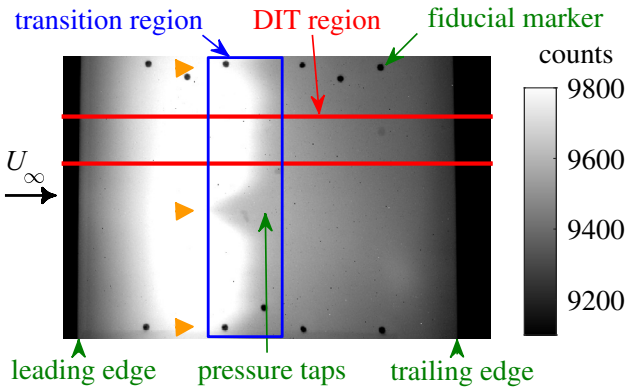


**Fig. 4** Infrared image for a static test case, $\alpha = 1.5°$

flux was measured with a power meter and is roughly 1500 W/m$^2$ over $0 \le x/c \le 0.5$ reducing to 420 W/m$^2$ at the trailing edge. This results in a temperature difference of 10–12 K between the airfoil's upper surface and the freestream temperature for dynamic test cases. In constant-pitch test cases, the heating was reduced to a temperature difference between 5 and 6 K.

An instantaneous IR image for a static test case with $\alpha = 1.5°$ is shown in Fig. 4, the flow direction is from left to right. The infrared intensity of the airfoil's surface is in the range of 9000–10000 counts. The conversion factor is between 8.4 mK/count at $T = 299$ K and 50 mK/count at $T = 320$ K with a noise equivalent temperature difference of 35 mK, see Gardner et al. (2016). However, the camera images were not temperature-calibrated, since the DIT method does not depend on absolute levels. The following sections use the infrared intensity measured in "counts" as a synonym for the surface temperature $T$.

In Fig. 4, both leading and trailing edges can be identified as vertical lines against the dark background. An automated detection of the edges is used to map the chordwise coordinate $x$ in instantaneous images. The transition region is marked by the blue rectangle, in which the intensity gradually decreases due to the increasing convective heat transfer in the turbulent boundary layer. The transition is slightly closer to the leading edge in three small spanwise regions marked by orange arrow markers, this results from an increased surface roughness due to pressure taps (central region) or silver-paint fiducial markers (upper/lower region). The area used for DIT evaluation is marked by red horizontal lines, and it covers 70 pixel (about 0.037 m) in the spanwise direction. The transition was found to be two-dimensional in this area, and the infrared signal will later be averaged along this direction to reduce the camera noise.

## 3 Data processing and results

### 3.1 IT and DIT for static test cases

Static-pitch test cases serve as a reference for the unsteady cases and demonstrate both the general idea of DIT and its validity under steady conditions. It is expected that the surface temperature $T$ of the heated airfoil is predominantly governed by the forced convective heat transfer. The Reynolds analogy connects the heat flux $\dot{q}_c$ to the friction drag coefficient $c_f$, see Truckenbrodt (2008):

$$\dot{q}_c = \frac{c_f}{2} \cdot C \cdot \rho \cdot V_\infty \cdot (T - T_\infty), \tag{2}$$

with the fluid's heat capacity $C$ and density $\rho$, and with the freestream velocity $V_\infty$ and temperature $T_\infty$. Assuming that at thermal equilibrium $\dot{q}_c$ equals a constant incoming heat flux of the spotlights and that other mechanisms of heat transfer have a minor influence, the surface wall temperature $T$ is inversely proportional to $c_f$.

The coefficient $c_f$ was estimated using viscous boundary-layer solutions provided by the 2D Euler solver MSES (Drela 1990), since the skin friction was not directly measured in the current experiments. The square symbols in Fig. 5 (top) correspond to the measured distributions of the pressure coefficient $c_p$ for two different static angles of attack. The lift coefficient $c_l$ was determined using the DLR in-house tool "cp2cl", which performs a first-order direct integration along the airfoil surface, accounting for the pressure taps, as shown in Fig. 1. This yields $c_l = 0.22$ for $\alpha = 4°$ and $c_l = 0.36$ for $\alpha = 7°$. The MSES solutions were calculated for the same $c_l$ values, see the solid lines in Fig. 5 (top). They are in reasonable agreement to the experimental results. It is noted that the corresponding MSES angles of attack are smaller than the experimental values due to 3D- and wind-tunnel wall interference or blockage effects.

The boundary layer transition on the airfoil's upper surface can be seen by the small kinks in the pressure distribution, see the blue and green arrow markers, whereas the lower surface is almost fully laminar. The MSES results for

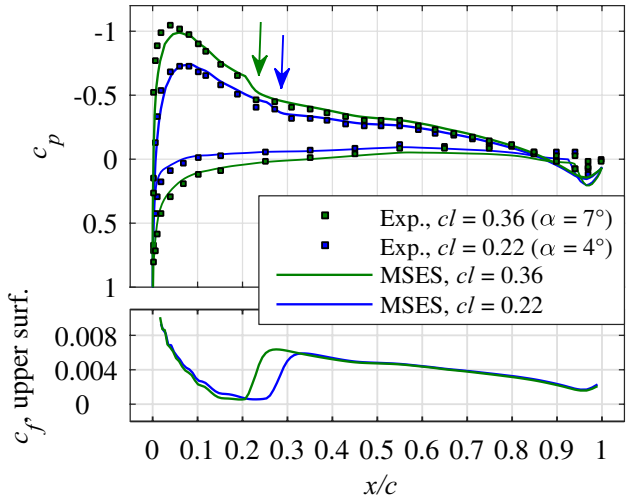


**Fig. 5** Pressure coefficient $c_p$ (top) and upper surface friction coefficient $c_f$ (bottom) for static $\alpha$

$c_f$ are shown in Fig. 5 (bottom). The skin friction strongly decreases in the laminar region starting at the leading edge. It sharply increases in the transitional region between about $0.20 < x/c < 0.34$ depending on $\alpha$, and then slightly decreases in the fully turbulent regime towards the trailing edge. The $c_f$ distributions for $\alpha = 4°$ and $\alpha = 7°$ are very similar except for the upstream motion of the transition. This illustrates the basic idea of DIT, see Raffel and Merz (2014) and Raffel et al. (2015), which assumes that the transition motion is the dominant source of temperature changes in the infrared images.

The time- and spanwise-averaged surface temperature distribution as measured in the DIT region for $\alpha = 4°$, see Fig. 6, has an inverse trend to the corresponding $c_f$ -distribution. This underlines the applicability of Eq. (2). The temperature strongly increases in the laminar region, $x/c < 0.26$, but then sharply drops in the transitional region, $0.26 \leq x/c \leq 0.34$. Further downstream the temperature is nearly constant up to about $x/c = 0.5$ and then slowly decreases towards the trailing edge. The last part contrasts with the slightly decreasing $c_f$ in the fully turbulent boundary layer and is caused by an inhomogeneous and decreasing radiative heating. Nevertheless, the tangents in the laminar, transitional, and turbulent regime can be determined, see the gray lines in Fig. 6. Using the method of Schülein (2008), the intersections of these lines correspond to the start and end of the transition region, with a 50% intermittence in its geometric center. For the current data, this point is also in a very good agreement to the location of the steepest temperature gradient $\mathrm{d}T/\mathrm{d}x$. The procedure of static transition detection for an individual pitch angle is termed "infrared thermography" (IT) in the following.

Static polar data were acquired with a stepping of $\Delta\alpha = 0.5°$, and the resulting lift coefficient $c_l$ is given in Fig. 7 as a function of the angle of attack $\alpha$.

Figure 8 (top) shows four pairs of temperature distributions between $\alpha = -2°$ and $\alpha = 7.5°$ with the transition moving upstream for an increasing angle of attack. Note that for $\alpha = -1.5°$ and $-2°$ (red lines), an exact localization of the transition region using IT is somewhat ambiguous due to its large streamwise extent and its proximity to the trailing edge.

The IT result for the entire $\alpha$-polar is shown in Fig. 9. The 50% intermittence point is represented by a green line. Its motion towards the leading edge is fast in the region of about $-1° \leq \alpha \leq 2.5°$ or $0.75 \geq x/c \geq 0.4$. This results from the flat pressure distribution and the small pressure gradients $\mathrm{d}c_p/\mathrm{d}x$ in this chordwise area, e.g., see Fig. 5 (top). The blue symbols in Fig. 9 correspond to the identified transition locations as seen by the $\sigma C_p$ method, which evaluates the cycle-to-cycle standard deviation of the dynamic pressure transducers (Gardner and Richter 2015). The $\sigma C_p$ results are mostly within the IT transition region (gray lines) but slightly upstream of the 50% intermittence point, with a deviation between about 1 and 4% of the chord length.

Applying the idea of DIT to static data, the temperature difference $\Delta T$ of two measurements with a separation of $\Delta\alpha = \alpha_2 - \alpha_1 = 0.5°$ is calculated, as shown in Fig. 8 (bottom).

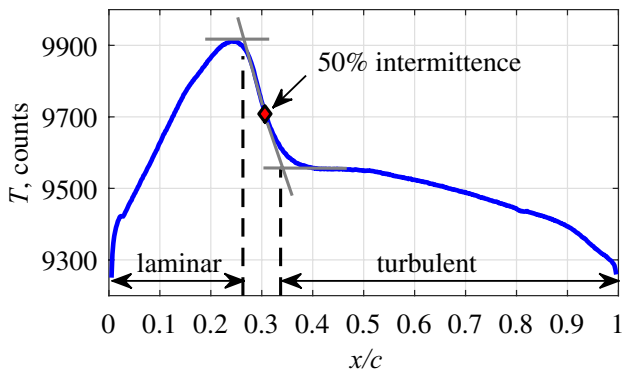


**Fig. 6** Temperature distribution, $\alpha = 4°$

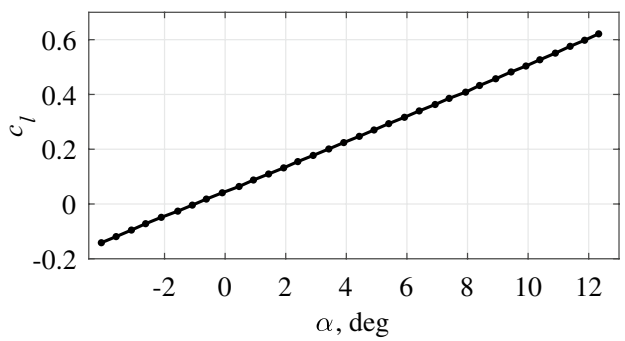


**Fig. 7** Lift coefficient for static angles of attack

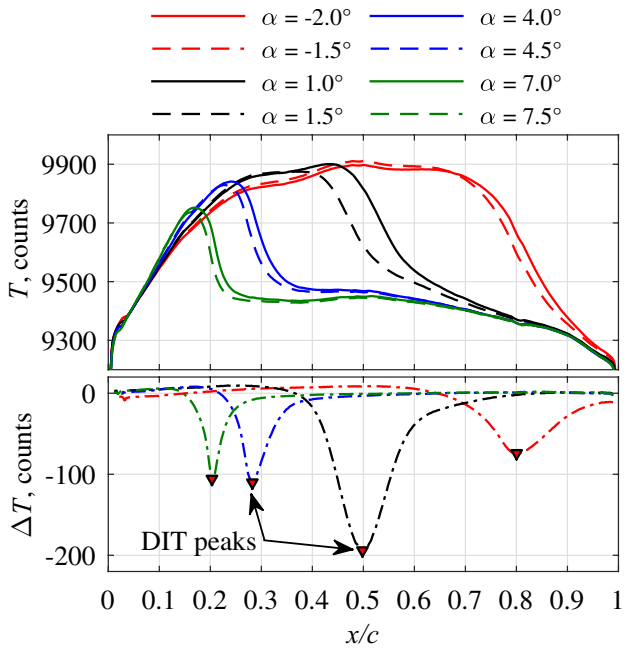


**Fig. 8** Intensity profiles (top) and DIT (bottom) for static-pitch angles $\alpha$

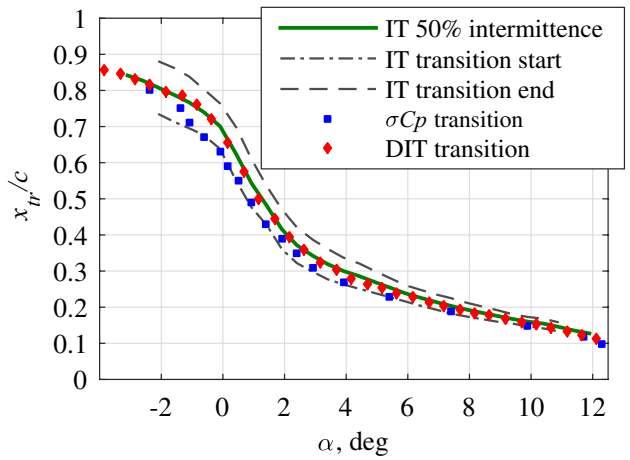


**Fig. 9** Transition versus $\alpha$ for IT, $\sigma C_p$, and DIT

The static data are assumed to be void of both aerodynamic and thermal hysteresis effects. The distributions have negative peaks, since $\alpha_2 > \alpha_1$, that is, the larger heat convection of the turbulent boundary layer moves towards the leading edge. Following the argumentation of Richter et al. (2016b) and Gardner et al. (2017), the peak position relates to the transition position $x_{tr}$ of the average angle:

$$\alpha = \frac{\alpha_1 + \alpha_2}{2}. \tag{3}$$

This is verified in Fig. 9, in which the 50% intermittence position for IT (green line) and the transition position for DIT (red diamond marker) agree within 1% of the chord length.

The negative DIT peak height $\Delta T_p$ is shown in Fig. 10 as a function of the angle of attack after Eq. (3) for the static polar. The peak height is not analyzed quantitatively during DIT processing, but it determines the signal-to-noise ratio of the peak position detection, which will be crucial in later dynamic test cases.

For steady-state DIT, it can be shown that the peak value $\Delta T_p$ linearly scales with the transition motion, $\Delta(x_{tr}/c)$, and the steepness of the temperature distribution at the transition location, $\mathrm{d}T/\mathrm{d}(x/c)_{x=x_{tr}}$. Consequently, large DIT peaks exceeding $-200$ counts are observed between $-0.5°$ and 2°, where the transition moves quickly in the upstream direction. At larger angles of attack $\alpha > 2°$, the transition motion is smaller and decreases towards the leading edge, which in combination with a slightly increasing steepness of the temperature distribution results in an almost constant peak level $\Delta T_p$ around $-100$ counts. For $\alpha < -1°$, both the transition motion and the steepness of the temperature distribution decrease, which yields a diminishing DIT peak signal towards the trailing edge.

## 3.2 DIT for pitching test cases

### 3.2.1 General procedure

The application and interpretation of DIT are more complex in pitch-oscillating test cases due to aerodynamic and thermal hysteresis effects. Figure 11 shows the instantaneous temperature distributions at the minimum and maximum pitch angles for sinusoidal motions with $\alpha = 4° \pm 3°$, $V_\infty = 50\,\mathrm{m/s}$, and three different reduced frequencies $k = 0.005, 0.009, 0.038$ (0.25 Hz, 1 Hz, 2 Hz). Arbitrary offsets were added to the graphs to improve the readability of the figure. For reference, also the static case $k = 0$ is repeated from Fig. 8. Note that the heating of the

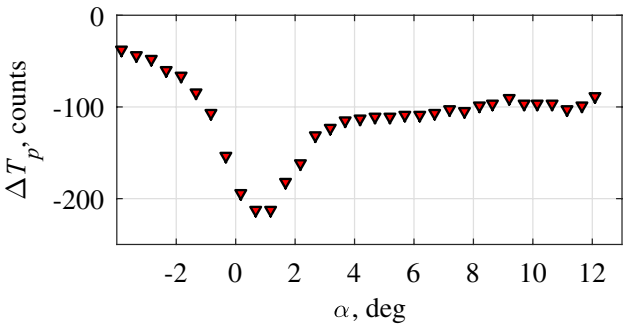


**Fig. 10** DIT peak height for static tests, $\Delta\alpha = 0.5°$

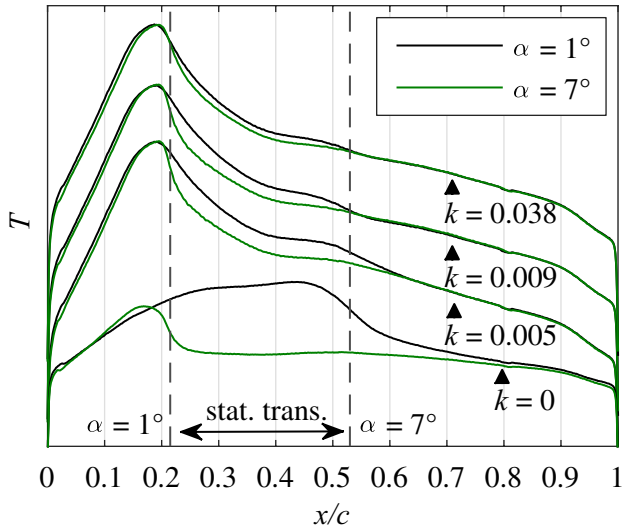


**Fig. 11** Intensity profiles for $\alpha = 4° \pm 3°$ and pitching frequencies $k = 0, 0.005, 0.009, 0.038$

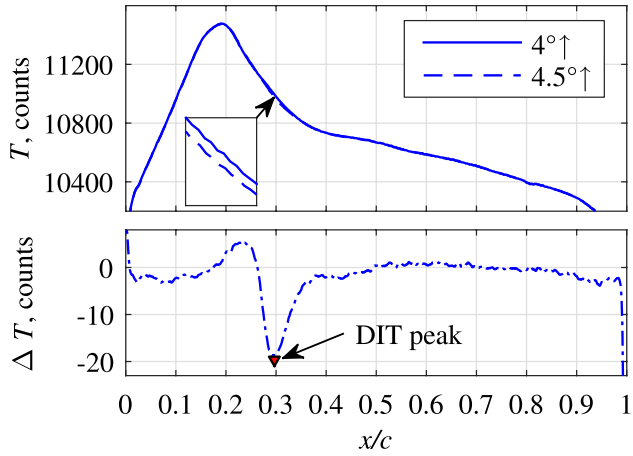


**Fig. 12** Intensity profiles (top) and DIT (bottom), $\alpha = 4° \pm 3°$, $k = 0.038$

static case was lower (see Table 1), which can be seen by a reduced temperature gradient $dT/dx$ in the area of the leading edge.

In the expected region of the transition movement between both pitch angles, circa $x/c = 0.22$–$0.53$ (dashed vertical lines), the temperatures for $\alpha = 7°$ (green lines) differ from the temperatures for $\alpha = 1°$ (black lines). However, even for the lowest frequency of $k = 0.005$ (0.25 Hz), this difference is much smaller than in the static case despite the higher heating. With increasing frequency $k$, the temperature differences further decrease, meaning that the temperature at a given $x/c$ approaches a constant level between the laminar and turbulent temperatures due to the limited thermal responsiveness of the model surface. Therefore, the instantaneous transition position and the overall temperature distribution are decoupled, and steady-state transition detection methods relying on the spatial temperature gradient (for example, as shown in Fig. 6) fail. Nevertheless, Gardner et al. (2017), Raffel and Merz (2014), Raffel et al. (2015), and Richter et al. (2016b) prove that the transition still results in meaningful temporal temperature gradients, which motivates the application of DIT.

Figure 12 (top) shows the temperature profiles for the $k = 0.038$-case (2Hz) at $\alpha = 4° \uparrow$ and $4.5° \uparrow$ during the upstroke, and the difference is barely visible in this scaling. A subtraction reveals the negative DIT peak which is discernible against the background noise level, see Fig. 12 (bottom). This dynamic $\Delta T$-distribution can be compared to the respective static result with $\Delta\alpha = 4.5° - 4°$, see the dashed–dotted blue graph in Fig. 8. The dynamic peak height is less than 20% of the static value, − 20 counts versus − 110 counts, due to the thermal inertia of the model surface.

The next step evaluates a pitch motion with $\alpha = 4° \pm 7°$, in which the transition motion covers large parts of the airfoil. Both the aerodynamic and thermal hysteresis are considerable when choosing $k = 0.075$ (4 Hz). Up to this point, the DIT was always calculated for an angle-of-attack difference of $\Delta\alpha = 0.5°$. This value cannot be kept constant for sinusoidal motions, since the pitching velocity varies as a function of the phase $tf$ and approaches zero at the upper and lower reversal points. Therefore, and in agreement with Raffel and Merz (2014), Raffel et al. (2015), and Richter et al. (2016b), a constant phase difference was chosen for DIT processing. The current example uses a separation of $\Delta tf = 0.01$ resulting in angle-of-attack differences $\Delta\alpha$ with a maximum of 0.5° (upstroke) and a minimum of −0.5° (downstroke). The 5000 infrared images of the test case are sorted in ascending phase, and for each image pair with $t$ and $t + \Delta t$, the DIT peak is detected, as shown in Fig. 12. The peak search region was restricted to ± 0.25 chord lengths around the corresponding static transition position, and this choice includes hysteresis effects, but removes some outliers.

Figure 13 shows the raw DIT data versus the pitch phase $tf$ as black dots, together with the angle of attack scaled between 0 and 1 as a gray dashed line. The transition position $x_{tr}$ can be unambiguously identified during large parts of the up- and downstroke. Towards the reversal points, unreliable data are expected, since the DIT separation $\Delta\alpha$ and the transition motion approach zero. This can be seen by means of moderate data scatter around $tf = 0.5$, at the upstream reversal of the transition motion. For $tf < 0.16$ and $tf > 0.90$, corresponding to the downstream reversal, large data scatter outweighs the valid DIT transition results. In this area, the decreasing DIT separation combines with the decreasing temperature differences towards the trailing edge, which was already shown in the static data (Fig. 10) to effectively prevent DIT evaluation.

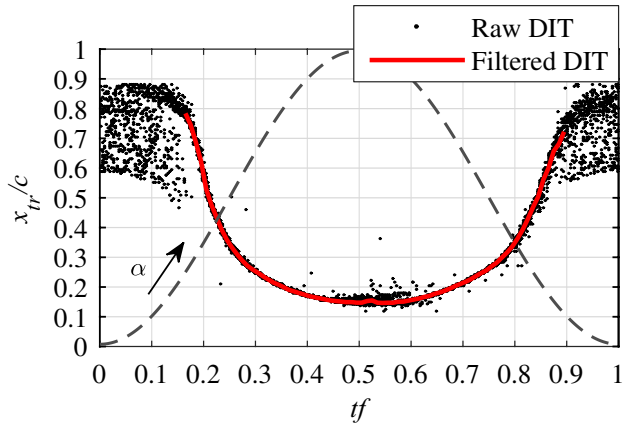


**Fig. 13** DIT result, $\alpha = 4° \pm 7°$, $k = 0.075$

The raw transition data were filtered using a similar approach as in Richter et al. (2016b). The data points are sorted in 100 equidistant bins along the phase $tf$ and the median of $x_{tr}$ is calculated for each bin, see the red line in Fig. 13. The standard deviation of the bins represents the local magnitude of data scatter. This value can be taken as a criterion to identify invalid data. An arbitrary threshold of 5% was used in the current case, which excludes unreliable data at the lower pitch reversal from further evaluation.

In Fig. 14, the filtered DIT result (red line) is plotted versus the angle of attack $\alpha$, revealing a hysteresis between the up- and downstroke of the motion which is approximately symmetric to the static transition position (gray line).

The $\sigma C_p$-procedure (blue rectangular symbols) has a smaller hysteresis. This indicates that DIT introduces a measurement-related lag in addition to the aerodynamic hysteresis. A detailed analysis of this effect will be presented in Sect. 3.3. On the average, the transition locations measured by $\sigma C_p$ are further upstream in comparison with DIT, which corresponds to the static results (Fig. 9) and most probably results from the surface disturbances of the pressure taps.

### 3.2.2 Compensation of temperature drift

The current de-tuning of the camera acquisition and pitching frequencies, see Sect. 2, means that the DIT separation can be chosen as integral multiples of the minimum value $\Delta tf = 2 \times 10^{-4}$. On the downside, two images with a small phase difference may have a large wall-clock time difference, which raises the question of the influence of temperature drift. This is demonstrated for the test point of the previous section, $\alpha = 4° \pm 7°$ at $k = 0.075$. Figure 15 shows the temperature drift as function of $x\,/\,c$ and the test time with a total duration of about 50 s. The drift was determined using a temporal low-pass filter which applies a sliding average window twice as large as the pitching period. By tendency, the area between $x/c = 0.1$ to 0.2 cools down, whereas the area between $x/c = 0.3$ to 0.9 heats up. This non-uniform evolution is unlikely to be caused by a drift of the freestream flow temperature or the heating intensity. It is more likely that the surface of the airfoil was not in a thermal equilibrium at the start of the test point, even though the pitch motion was turned on prior to the first infrared image for about 20–30 s required for a fine-tuning of the motion controller. A similar drift is found in the majority of the current test points, indicating that it is a general problem and that the thermal inertia of the model surface is too large to wait for equilibrium under the constraints of limited wind-tunnel time. A drift of ten counts corresponds to roughly 0.5 K over 50 s of test time. Gardner et al. (2017) suggest that roughly 10 min of wait time after setting the motion would reduce this drift by a factor of 10.

The temperature drift can be compensated through a subtraction of the low-pass filtered signal. Figure 16 shows the DIT differential temperature distribution at a phase

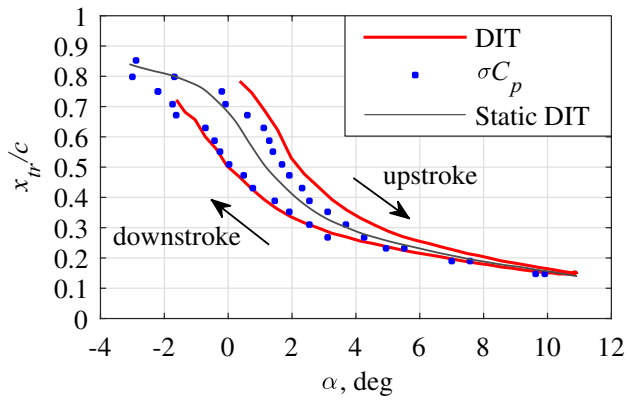


**Fig. 14** $x_{tr}$ versus $\alpha$, $\alpha = 4° \pm 7°$, $k = 0.075$

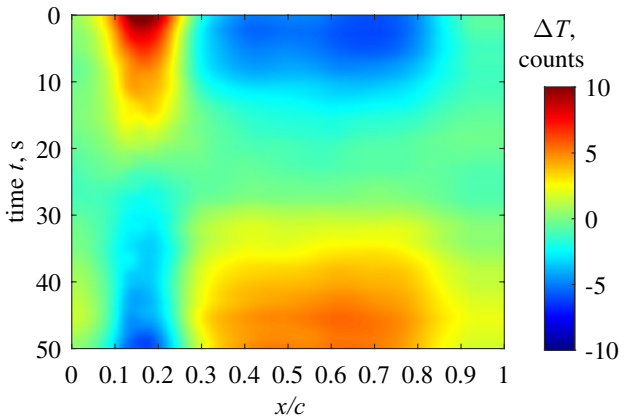


**Fig. 15** Sample temperature drift of the airfoil

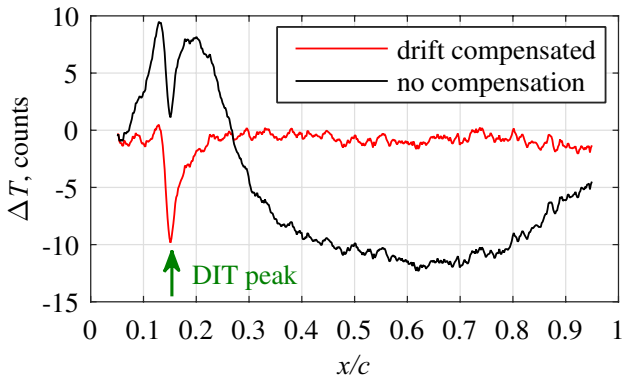


**Fig. 16** Example for DIT temperature compensation

of $tf = 0.47$ ($\alpha = 10.9° \uparrow$). The chosen phase separation $\Delta tf = 0.01$ of the two underlying infrared images is small, but the wall-clock time separation is large, about 39 s. In the temperature-compensated DIT (red line), a single negative DIT peak at $x/c = 0.15$ clearly marks the transition motion. In the non-compensated DIT (black line), the same transition peak is superimposed with a strong temperature drift. The DIT peak is distorted and hardly detectable by automated algorithms, and its position is slightly biased. Therefore, DIT results discussed in the previous and next sections are corrected for the temperature drift, without further notice.

### 3.3 Influence of DIT separation

Gardner et al. (2017) showed that the separation distance $\Delta tf$ between two temperature distributions processed by DIT has a decisive influence on the quality of the results. Smaller separations result in smaller lags between the measured and the true transition positions, since the influence of the airfoil's thermal inertia is reduced. On the other hand, also the DIT peak height, and therefore, the signal-to-noise ratio is reduced. The effects will be studied in more detail by revisiting the reference test case of Sect. 3.2.1, $\alpha = 4° \pm 7°$ at $k = 0.075$.

Figure 17 shows the unfiltered DIT results for the separations $\Delta tf = 0.005$ (top, green symbols) and $\Delta tf = 0.05$ (bottom, blue symbols). The results are generally similar, but the smaller separation yields a larger scatter. This can be explained by the corresponding $\Delta T$ peak heights shown in Fig. 18. As expected from the larger convective heat transfer in the turbulent boundary layer, the peaks have a negative sign (cooling) when the transition moves forward and a positive sign (heating) when the transition moves backward. The higher separation (blue symbols) results in distinct DIT peaks of up to about $\pm 50$ counts, whereas the peaks of the smaller separation (green symbols) are at the edge of the noise limit, which is about $\pm 5$ counts for the current infrared imaging setup.

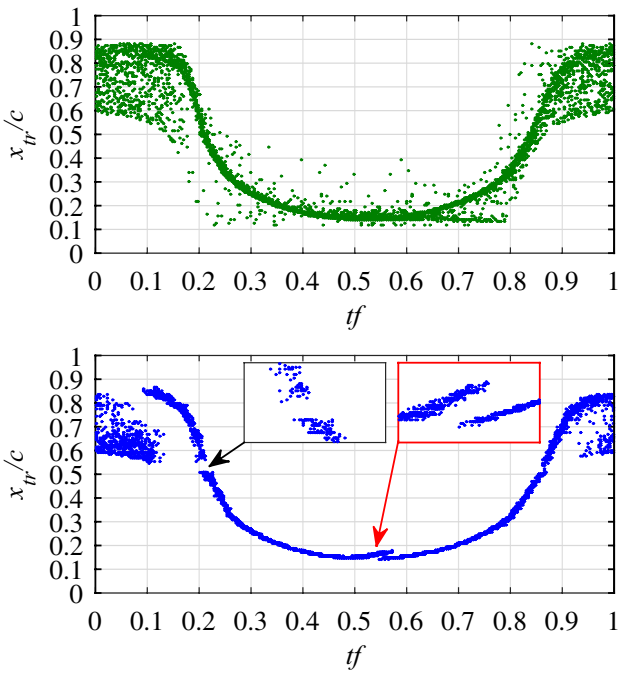


**Fig. 17** DIT for $\alpha = 4° \pm 7°$, $k = 0.075$, DIT separations $\Delta tf = 0.005$ (top) and $\Delta tf = 0.05$ (bottom)

Apart from the higher signal-to-noise ratio, the DIT transition position of the large $\Delta tf$, see Fig. 17 (bottom), has three discontinuities which do not occur for the small $\Delta tf$. Two voids are formed during the up- and downstroke at about $tf = 0.21$ and $tf = 0.86$, the former region is shown in the black-framed detail. At this point, the choice of $\Delta tf = 0.05$ results in a large pitch difference of $\Delta\alpha = 2.4°$ and a large transition motion of more than 0.3 chord lengths. The corresponding differential temperature distribution is shown as the black line in Fig. 19. The DIT peak is not only very broad due to the large transition motion, but it begins to split up into two separate peaks with a dent in between. This violates the single-peak assumption of the DIT method.

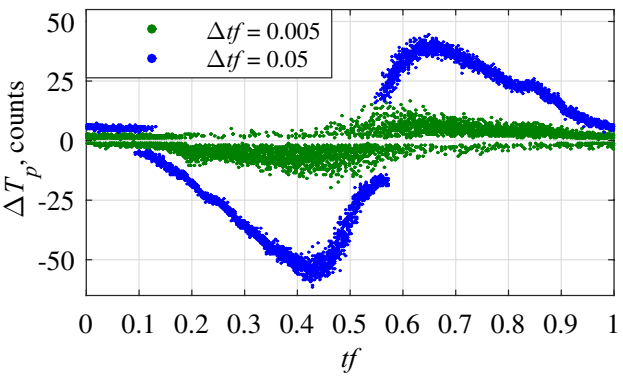


**Fig. 18** DIT peak height, $\Delta tf = 0.005$ and 0.05

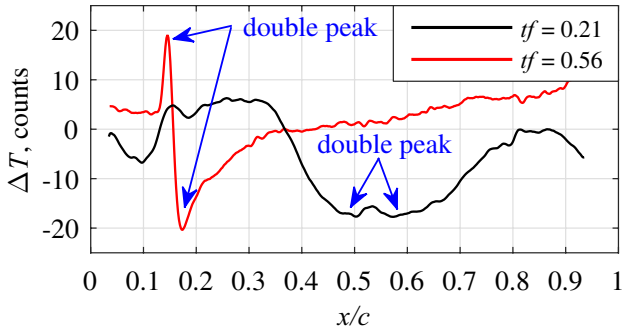


**Fig. 19** Erroneous DIT results, $\Delta tf = 0.05$

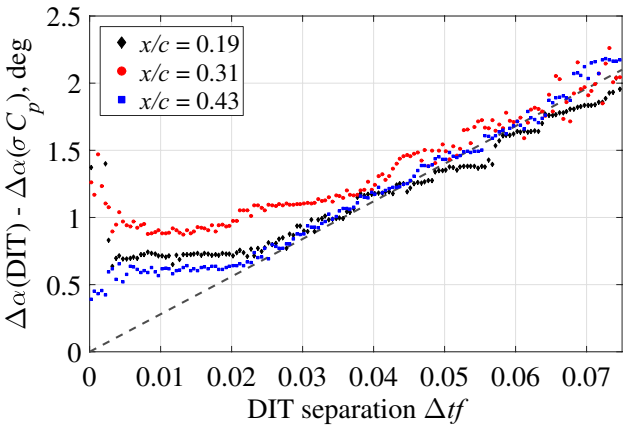


**Fig. 20** Difference between DIT and $\sigma C_\mathrm{p}$ hysteresis as function of $\Delta tf$, $\alpha = 4° \pm 7°$ at $k = 0.075$

The detected peak positions randomly switch between both double peaks, forming a void in the result data between $x_\mathrm{tr}/c = 0.52$ and 0.53. It is noted that the same effect can also be observed when increasing the pitch difference of the static DIT evaluation from $\Delta\alpha = 0.5°$ to values larger than $\Delta\alpha = 2°$, even though this was not discussed in Sect. 3.1.

The third gap in the results for $\Delta tf = 0.05$ occurs at the upstream reversal point of the transition, about $tf = 0.56$. It is shown by the red-framed detail in Fig. 17 (bottom). This phenomenon was first discovered by Richter et al. (2016b) and studied in more detail by Gardner et al. (2017). The sign of the DIT peak switches from negative to positive at the reversal point. Both states are coexistent due to the thermal hysteresis particularly for large DIT separations, and again, the double-peak structure in the temperature difference yields erroneous results. This is shown by the red line in Fig. 19. The current evaluation detects the temperature peak regardless of its sign, i.e., as the maximum value of $\Delta T$. Therefore, the peak position randomly switches between the positive and negative peaks. Gardner et al. (2017) suggest that the peak search algorithm should be modified to differentiate between forward motion (negative peak) and backward motion (positive peak). This requires apriori knowledge of the exact transition reversal point, which lags behind the pitch reversal. The current work shows that instead, the DIT separation can be reduced up to a point, where this double-peak effect merges into the general noise level, see Figs. 13 and 17 (top). It is noted that the same problems are also expected at the rearward motion reversal (Gardner et al. 2017). This cannot be observed in the current pitch motion, since the signal-to-noise ratio towards the trailing edge is too low even for very large DIT separations.

Finally, the effect of the DIT separation $\Delta tf$ on the measured hysteresis is studied. The angle of attack in which the transition crosses a certain location $x/c$ is determined for both up- and downstroke of the pitch motion. The deviation between both values, $\Delta\alpha = \alpha\uparrow - \alpha\downarrow$, is taken as a measure for the hysteresis, corresponding to the horizontal distance between up- and downstroke in Fig. 14. In addition, the hysteresis calculated by $\sigma C_\mathrm{p}$ is subtracted from the respective DIT result, assuming that the fast-response $\sigma C_\mathrm{p}$ method is close to the true aerodynamic hysteresis. The difference, therefore, represents the additional measurement hysteresis or thermal lag which is introduced by DIT. This additional measurement hysteresis is shown in Fig. 20 for three transition locations $x/c = 0.19, 0.31, 0.43$ and multiple separation distances up to 0.075 of the pitch period. All three graphs decrease approximately linearly from about $\Delta tf = 0.075$ to $\Delta tf = 0.03$. The extension of this trend is shown as a dashed gray line which crosses the origin.

This behavior was predicted in the DIT simulations by Gardner et al. (2017), which imply that the measurement-related delay approaches zero when the separation distance is reduced. In contrast to this prediction, the measured lags in Fig. 20 successively level out for separations smaller than $\Delta tf = 0.03$, and assume an almost constant DIT-to-$\sigma C_\mathrm{p}$-offset between 0.5° and 1° for $\Delta tf < 0.02$. The largest offset occurs at $x/c = 0.31$, which approximately corresponds to the mean angle of attack and the highest pitching velocity of the sinusoidal motion. This relation will be evaluated in more detail in the next section. For very small separations, $\Delta tf < 0.005$, the results are affected by random scatter. This can be explained by the diminishing signal-to-noise ratio of the DIT peak already discussed in Fig. 18. In summary, the current test case yields a non-zero DIT measurement lag error. It can be minimized when choosing separations in the range of $\Delta tf = 0.005 \ldots 0.02$, but it cannot be eliminated. This motivates the discussion of different pitching frequencies, $k$, since it is known from Sect. 3.1 that DIT converges to the "true" IT results for static cases with $k = 0$.

### 3.4 Discussion of pitch frequency and pitch amplitude effects

The DIT transition positions for different pitching frequencies between $k = 0.005$ (0.25 Hz) and $k = 0.151$ (8 Hz) are shown in Fig. 21. The mean and amplitude of the motion, $\alpha = 4° \pm 6°$, and the DIT separation of $\Delta tf = 0.01$ were kept constant. Expectedly, the hysteresis between the up- and downstroke increases with increasing $k$, which includes both aerodynamic and measurement-related lag effects. The transition detection towards the rearward reversal point is better when reducing the pitch frequency, this is caused by an increasing signal-to-noise ratio for slower transition motions.

The influence of the DIT separation $\Delta tf$ on the DIT measurement lag, see Fig. 22, is very similar to the reference case (Fig. 20). The optimal separation between about $\Delta tf = 0.005$ and 0.02 is independent of $k$, and it is bounded by large scatter at smaller $\Delta tf$ and an increasing measurement lag at higher $\Delta tf$. Smaller pitch frequencies generally yield a smaller irreducible measurement lag, see the black arrow in Fig. 22. This trend is shown by all $k$ values except for $k = 0.151$. It is noted that the uncertainty in the data is partly introduced by the scatter of the $\sigma C_p$-hysteresis, which was subtracted from the DIT results.

Figure 23 shows the DIT transition results for pitch motions with a constant mean angle of $\overline{\alpha} = 4°$ and a constant frequency of $k = 0.075$, but a varying amplitude between $\hat{\alpha} = 3°$ and $\hat{\alpha} = 8°$. The amplitude defines the extent of the transition motion but also its speed and hysteresis, with larger $\hat{\alpha}$ resulting in larger lags. This is due to the effect of $\hat{\alpha}$ on the pitch velocity, which can be derived from the formulation of the angle of attack in Eq. (1):

$$\frac{\mathrm{d}\alpha}{\mathrm{d}t} = 2\pi f \hat{\alpha} \cdot \sin(2\pi\, tf). \tag{4}$$

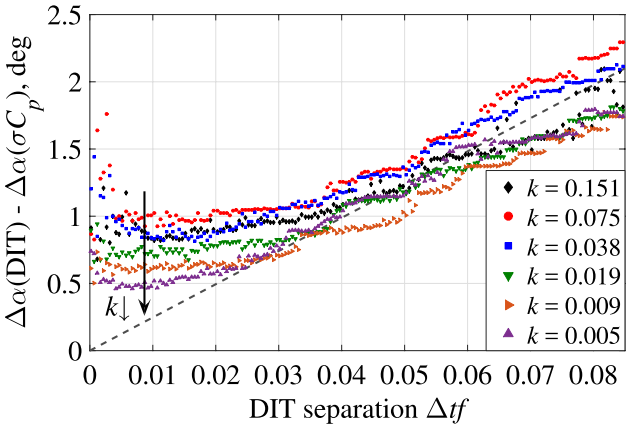


**Fig. 22** Difference between DIT and $\sigma C_p$ hysteresis at $x/c = 0.31$ as a function of $\Delta tf$, $\alpha = 4° \pm 6°$

A more comprehensive overview is, therefore, achieved by varying both pitch frequency and amplitude. The results are then evaluated as a function of the pitch velocity.

The hysteresis $\Delta\alpha$ is studied at $x/c = 0.31$, which is close to the transition position of the mean angle $\overline{\alpha} = 4°$ (see Fig. 9) and which is equipped with a pressure tap. This means that the DIT-to-$\sigma C_p$ comparison can be conducted for the entire parameter range of Table 1. The pitch velocity is calculated by averaging the two values for $\mathrm{d}\alpha/\mathrm{d}t$ at which the transition crosses $x/c = 0.31$ during the up- and downstroke. Both values are close to the mean pitch angle and, therefore, close to the maximum velocity value of $2\pi f\hat{\alpha}$ (Eq. 4).

The individual hysteresis of both techniques is shown as filled symbols in Fig. 24 (top). The colored symbols belong to DIT and the gray symbols belong to $\sigma C_p$. Two data points with the same filled marker symbols have the same frequency $k$ but a different amplitude $\hat{\alpha}$. The pitching velocity is apparently the correct scaling parameter, at

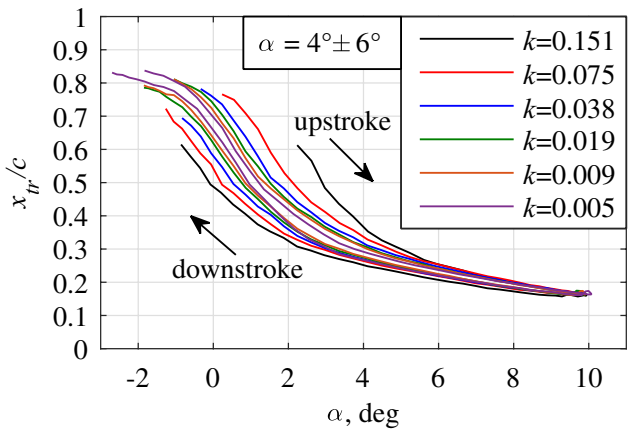


**Fig. 21** DIT transition results, variation of the pitch frequency $k$ for $\alpha = 4° \pm 6°$

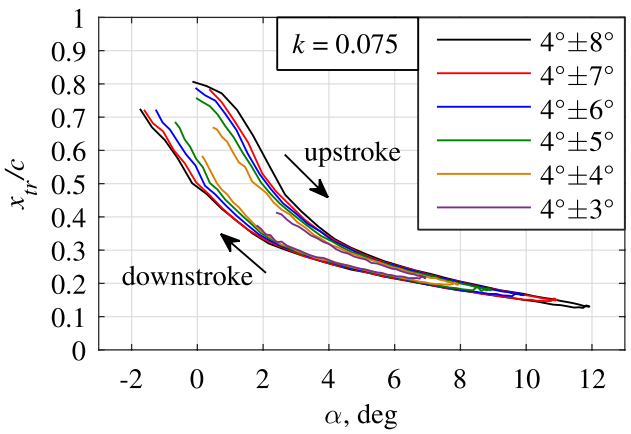


**Fig. 23** DIT transition results, variation of the pitch amplitude $\hat{\alpha}$ for $\overline{\alpha} = 4°$ and $k = 0.075$

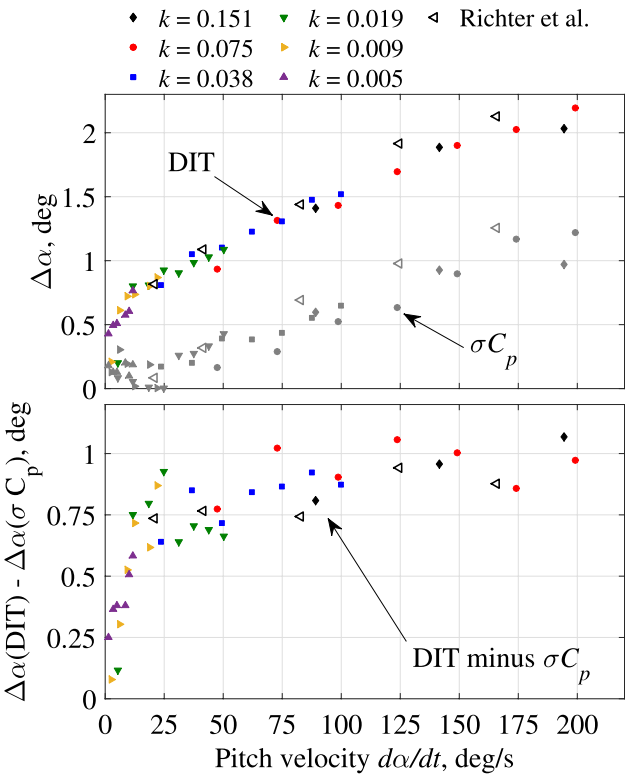


**Fig. 24** Transition hysteresis of DIT and $\sigma C_p$ at $x/c = 0.31$ (top) and difference between both (bottom) as function of the pitch velocity. Unfilled symbols are data taken from Richter et al. (2016b)

least for a given transition location. This is evident regarding the clear trend and the low scatter of the DIT data points. The $\sigma C_p$-reference always has a smaller hysteresis than DIT, and $\Delta\alpha$ decreases with $d\alpha/dt$ roughly linearly towards zero, which is expected for the true aerodynamic hysteresis. The behavior of DIT is easier to understand when subtracting the respective $\sigma C_p$ values. The result is shown in Fig. 24 (bottom), representing the additional DIT measurement lag. For pitch velocities between 15 and 200 deg/s, this error is scattered between 0.6° and 1.1 deg/s with a slightly rising trend. For pitch velocities smaller than 15 deg/s, a steep decrease towards zero lag can be seen, which is the expected result when approaching steady conditions.

The unfilled triangular symbols in Fig. 24 is data taken from Fig. 23 in Richter et al. (2016b), who studied the same airfoil model at $M_\infty = 0.3$, $Re = 1.8 \cdot 10^6$, and reduced frequencies between $k = 0.01$ and $k = 0.08$. The data agree well with the current results despite the different freestream conditions. Richter et al. applied a linear fit to the DIT data points and concluded that there is an offset at the zero frequency $k = 0$, which contradicts lag-free static infrared measurements. Figure 24 shows that Richter et al.'s smallest pitch rate of 20 deg/s is too large to capture the behavior towards $k \to 0$ correctly, but the current data close this gap towards static behavior.

## 4 Summary and conclusion

A comprehensive study of a pitching airfoil was conducted to optimize the differential infrared thermography for boundary layer transition detection. The main results are summarized as follows:

- DIT can also be applied in static test cases, and results in an improvement of the transition point detection for complex temperature distributions. The results are in good agreement with established steady-state infrared analysis methods, and DIT favors an unambiguous and automated evaluation procedure. The static results provide apriori estimates for the transition position in dynamic cases and thereby improve the peak search algorithm.
- The instantaneous temperature distribution within the transition-motion region of pitch-oscillating test cases is different from its static counterpart even at very low frequencies. The temperature approaches a phase-averaged state between laminar and turbulent states. This prevents the application of steady-state infrared transition detection, and for DIT yields a much smaller signal strength compared to static cases.
- A de-tuning of the infrared camera frequency and the pitch motion frequency can be used to achieve very fine phase resolutions for periodic motions.
- The DIT results are sensitive to spatially inhomogeneous temperature drift. It is advisable to identify and remove long-term temperature drift prior to DIT evaluation.
- For technically relevant pitch frequencies, the DIT procedure results in an additional measurement lag when compared to fast-response techniques. For the current case, this lag yields an additional angle-of-attack hysteresis, which is in the range of about 0.6° to 1.1° for a very wide range of pitching rates between 15 and 200 deg/s.
- The separation distance of the two infrared images subtracted during DIT processing is a crucial parameter which determines the quality of the results. Very large separations, corresponding to pitch differences above 2°, and the resulting transition motion yield "double-peak" structures which are easily misinterpreted as two different transition positions. For smaller separations a compromise between the minimization of the measurement lag and the maximization of the signal-to-noise ratio must be found. In the current case, best results were achieved for angular separations of about $\Delta\alpha = 0.5°$ or phase separations between $\Delta tf = 0.005$ and 0.02.

**Acknowledgements** The studies were conducted in the framework of the DLR project “FAST-Rescue”.

## References

Coder JG (2017) OVERFLOW rotor simulations using advanced turbulence and transition modeling. In: 55th AIAA aerospace sciences meeting, AIAA SciTech Forum, Grapevine, TX, USA, Jan 9–13, 2017. https://doi.org/10.2514/6.2017-1432

Drela M (1990) Newton solution of coupled viscous/inviscid multielement airfoil flows. In: AIAA 21st fluid dynamics, plasma dynamics and lasers conference, Seattle, WA, USA, June 18–20, 1990. https://doi.org/10.2514/6.1990-1470

Gardner AD, Richter K (2015) Boundary layer transition determination for periodic and static flows using phase-averaged pressure data. Exp Fluids 56(6):119. https://doi.org/10.1007/s00348-015-1992-9

Gardner AD, Richter K (2016) New results in numerical and experimental fluid mechanics X, Springer International Publishing, chap transition determination on a periodic pitching airfoil using phase averaging of pressure data, pp 291–301. https://doi.org/10.1007/978-3-319-27279-5_26

Gardner AD, Wolf CC, Raffel M (2016) A new method of dynamic and static stall detection using infrared thermography. Exp Fluids 57(9):149. https://doi.org/10.1007/s00348-017-2405-z

Gardner AD, Eder C, Wolf CC, Raffel M (2017) Analysis of differential infrared thermography for boundary layer transition detection. Exp Fluids 58(9):122. https://doi.org/10.1007/s00348-017-2405-z

Goerttler A, Gardner AD, Richter K (2017) New results in numerical and experimental fluid mechanics XI, Springer International Publishing, chap unsteady boundary layer transition detection by automated analysis of hot film data, pp 387–396. https://doi.org/10.1007/978-3-319-64519-3_35

Lorber PF, Carta FO (1992) Unsteady transition measurements on a pitching three-dimensional wing. In: Fifth symposium on numerical and physical aspects of aerodynamic flows, Long Beach, CA, USA, Jan 13–15, 1992

Merz CB, Wolf CC, Richter K, Kaufmann K, Mielke A, Raffel M (2017) Spanwise differences in static and dynamic stall on a pitching rotor blade tip model. J Am Helicopter Soc 62(1):1–11. https://doi.org/10.4050/JAHS.62.012002

Overmeyer A, Heineck JT, Wolf CC (2018) Unsteady boundary layer transition measurements on a rotor in forward flight. In: 74th annual forum of the American Helicopter Society, Phoenix, AZ, USA, May 14–17, 2018

Overmeyer AD, Martin PB (2017a) The effect of laminar flow on rotor hover performance. In: 73rd annual forum of the American Helicopter Society, Fort Worth, TX, USA, May 9–11, 2017

Overmeyer AD, Martin PB (2017b) Measured boundary layer transition and rotor hover performance at model scale. In: 55th AIAA aerospace sciences meeting, AIAA SciTech Forum, Grapevine, TX, USA, Jan 9–13, 2017. https://doi.org/10.2514/6.2017-1872

Raffel M, Merz CB (2014) Differential infrared thermography for unsteady boundary-layer transition measurements. AIAA J 52(9):2090–2093. https://doi.org/10.2514/1.J053235

Raffel M, de Gregorio F, de Groot K, Schneider O, Sheng W, Gibertini G, Seraudie A (2011) On the generation of a helicopter aerodynamic database. Aeronaut J 115(1164):103–112. https://doi.org/10.1017/S0001924000005492

Raffel M, Merz CB, Schwermer T, Richter K (2015) Differential infrared thermography for boundary layer transition detection on pitching rotor blade models. Exp Fluids 56(2):30. https://doi.org/10.1007/s00348-015-1905-y

Raffel M, Gardner AD, Schwermer T, Merz CB, Weiss A, Braukmann J, Wolf CC (2017) Rotating blade stall maps measured by differential infrared thermography. AIAA J 55(5):1753–1756. https://doi.org/10.2514/1.J055452

Richter K, Schülein E (2014) Boundary-layer transition measurements on hovering helicopter rotors by infrared thermography. Exp Fluids 55(7):1755. https://doi.org/10.1007/s00348-014-1755-z

Richter K, Schlein E, Ewers B, Raddatz J, Klein A (2016a) Boundary layer transition characteristics of a full-scale helicopter rotor in hover. In: 72nd annual forum of the American Helicopter Society, West Palm Beach, FL, USA, May 17–19, 2016

Richter K, Wolf CC, Gardner AD, Merz CB (2016b) Detection of unsteady boundary layer transition using three experimental methods. In: 54th AIAA aerospace sciences meeting, San Diego, CA, USA, Jan 4–8, 2016

Schreck SJ, Faller WE, Helin HE (1998) Pitch rate and reynolds number effects on unsteady boundary-layer transition and separation. J Aircr 35(1):46–52. https://doi.org/10.2514/2.2258

Schülein E (2008) Experimental investigation of laminar flow control on a supersonic swept wing by suction. In: 4th flow control conference, fluid dynamics and co-located conferences, Seattle, WA, USA, June 23–26, 2008. https://doi.org/10.2514/6.2008-4208

Schülein E (2014) Optical method for skin-friction measurements on fast-rotating blades. Exp Fluids 55(2):1672. https://doi.org/10.1007/s00348-014-1672-1

Tanner W, Yaggy P (1966) Experimental boundary layer study on hovering rotors. J Am Helicopter Soc 11(3):22–37. https://doi.org/10.4050/JAHS.11.22

Truckenbrodt EA (2008) Fluidmechanik Band 2: Elementare Strömungsvorgänge dichteveränderlicher Fluide sowie Potential- und Grenzschichtströmungen. Springer, Berlin

Vieira BA, Kinzel MP, Maughmer M (2017) CFD hover predictions including boundary-layer transition. In: 55th AIAA aerospace sciences meeting, AIAA SciTech Forum, Grapevine, TX, USA, Jan 9–13, 2017. https://doi.org/10.2514/6.2017-1665

Wadcock AJ, Yamauchi GK, Driver DM (1999) Skin friction measurements on a hovering full-scale tilt rotor. J Am Helicopter Soc 44(4):312–319. https://doi.org/10.4050/JAHS.44.312

Weiss A, Gardner AD, Klein C, Raffel M (2017) Boundary-layer transition measurements on mach-scaled helicopter rotor blades in climb. CEAS Aeronaut J 8(4):613–623. https://doi.org/10.1007/s13272-017-0263-2